Effects of Pearlite on Thermal Fatigue and Wear Resistance of Gray Cast Iron Treated by Laser

Dahui Yu, Ti Zhou, Hong Zhou, Peng Zhang, and Yuying Yan

In order to improve the thermal fatigue and wear resistance of gray cast iron, the effects of pearlite on thermal fatigue and wear resistance of gray cast iron were studied, the microstructure of different pearlite contents (45% to 85%) and interlamellar spacing were characterized by optical microscopy and scanning electron microscopy (SEM), the microhardness was measured by automatic microhardness tester, and the thermal fatigue and wear resistance of varying pearlite content and interlamellar spacing have been tested separately. Then, the 45° mesh double combination model was processed by pulse laser on the specimens' surfaces, and then thermal fatigue and wear tests were carried out. The finite element analysis software was used to investigate stress distributions during wear tests. The treated samples were compared with untreated samples afterward. The results show that due to the thermal fatigue and wear resistance of pearlite, samples with pearlite contents greater than or equal to 85%, and the samples with pearlite interlamellar spacing of 152nm, have the best thermal fatigue and wear resistance. After the laser treatment, the difference of pearlite contents and interlamellar spacing on thermal fatigue and wear resistance of gray cast iron was eliminated, which reduced the production cost and increased the service life of casting.

1. Introduction

Gray cast iron has been widely used in manufacturing such as brake drums, brake disks and cylinders of automobiles because of excellent properties like castability, shock absorption and wear resistance (Ref 1-3). The primary failure mode of brake drum is thermal fatigue cracks caused by friction heating during braking (Ref 4), as shown in Fig.1. With the continuous development of the economy, more and more rated loads are needed by trucks, which means the brake drum will bear a superior braking force. Due to the excellent cost performance, most trucks on roads still use gray cast iron brake drums instead of steel or other materials. In recent years, there are many examples of life and economic losses caused by overloading and driving in complicated mountain roads (Ref 5). Therefore,

the improvement in thermal fatigue and wear resistance of gray cast iron is not only related to economic benefits but also an important issue to protect life safety.

Many factors are affecting the thermal fatigue and wear properties of gray cast iron. It is well known that the continuous improvement in casting methods is aimed at obtaining high-quality cast iron (Ref 6-8). Yi et al. found that the more prolonged the graphite, the higher the stress at the tip of the graphite; this is the thermal–mechanical coupling characteristics of graphite morphology (Ref 9). The service life of gray cast iron is closely related to many factors, and Goo et al. found that the chemical composition and the microstructure of the cast iron could directly affect its service life (Ref 10). Laser melting is a technique that uses a high energy density laser beam to irradiate the surface of a material, forming a melt pool with a certain depth in the irradiated area, and after cooling, forming a refined tissue in the melted area and thus obtaining a high hardness and strength, thus enhancing the fatigue and wear resistance of the material (Ref 11, 12). Zhou et al. found that biological fatigue and wear-resistant surfaces in nature are mostly soft and hard structures. Using the coupling bionic idea as a reference, a similar bionic structure can be obtained by using laser melting techniques to model the material surface according to a certain amount of characteristics, which greatly enhances the fatigue and wear resistance of the material, and after studying point shape models, stripe models and mesh models, it was found that the surface samples with the mesh model had the most improved thermal fatigue and wear resistance (Ref 13, 14). Lu et al. studied the influence of graphite type on thermal fatigue behavior of laser-treated gray cast iron (Ref 15). Inspired by the failure characteristics of gray cast iron brake drums, Yu et al. designed a non-single model, in which the service life of brake drums is increased at least two times (Ref 16). Based on previous studies, we found that laser melting technology can effectively improve the thermal fatigue and wear resistance of gray cast iron, but the effects of pearlite on thermal fatigue and wear resistance of gray cast iron and the

Dahui Yu, Key Laboratory of Automobile Materials (Jilin University), Ministry of Education, Changchun 130025, People's Republic of China; School of Material Science and Engineering, Jilin University, Changchun 130025, People's Republic of China; and Faculty of Engineering, University of Nottingham, Nottingham NG7 2RD, UK; **Ti Zhou**, Key Laboratory of Automobile Materials (Jilin University), Ministry of Education, Changchun 130025, People's Republic of China; and School of Mechanical Science and Aerospace Engineering, Jilin University, Changchun 130025, People's Republic of China; **Hong Zhou** and **Peng Zhang**, Key Laboratory of Automobile Materials (Jilin University), Ministry of Education, Changchun 130025, People's Republic of China; and School of Material Science and Engineering, Jilin University, Changchun 130025, People's Republic of China; **Yuying Yan**, Faculty of Engineering, University of Nottingham, Nottingham NG7 2RD, UK. Contact e-mails: zhouti@jlu.edu.cn zhouti@jlu.edu.cn.

impact of laser melting technology have not been studied. In that case, we used the double combination model (shown in Fig.2) and processed it on the surface of specimens by a pulse laser to study pearlitic gray cast iron.

Pearlite is composed of alternating layers of ferrite and cementite (Ref 17). The comprehensive mechanical properties of pearlite are much better than that of ferrite or cementite alone (Ref 18, 19). The properties of a cast iron that contains pearlite are determined by the amount of pearlite and the interlamellar spacing of the pearlite. In this study, the pearlite in different areas of a brake drum was measured. According to the failure mechanism of the brake drum, the working surface was divided into three regions and the pearlite on both inside and surface was measured as well. The working surface of the brake drum is the contact surface between the brake drum and the brake pad. In order to improve the thermal fatigue and wear resistance of gray cast iron, a surface-treated pattern was fabricated using a laser on the surface of the sample, and the effect of the contents of pearlite and the interlamellar spacing of the pearlite on the thermal fatigue and wear resistance of laser-treated gray cast iron sample was investigated.

2. Materials and Methods

2.1 Material

Samples in this study were cut from a HT200 (ISO 200) gray cast iron brake drum (made by Fuhua Corporation, China); the company produces brake drums using the sand casting method. The brake drum is flanged to the bottom and gets thinner from the bottom up with the thickness range of 13-18mm. The graphite type of gray cast iron used in this study was measured by metallographic examination to be flake type A, size class 4 (160-320μm). The representative chemical composition of the brake drum is as follows (wt.%): Si 1.770, Mn 0.820, P 0.060, S 0.059, Cu 0.500, Cr 0.270 and C 3.450.

2.2 Preparation of Samples

The size of all samples is $40 \times 20 \times 6$ mm (Ref 3) made by an electrical discharge machine (EDM). In this study, the samples with varying pearlite contents were taken from the bottom up at a distance of 6 mm from the working surface of the brake drum, and the interlamellar spacing samples were taken from both the inside and the surface of the brake drum. All samples need to be machined with a round hole with a radius of 1 mm in order to
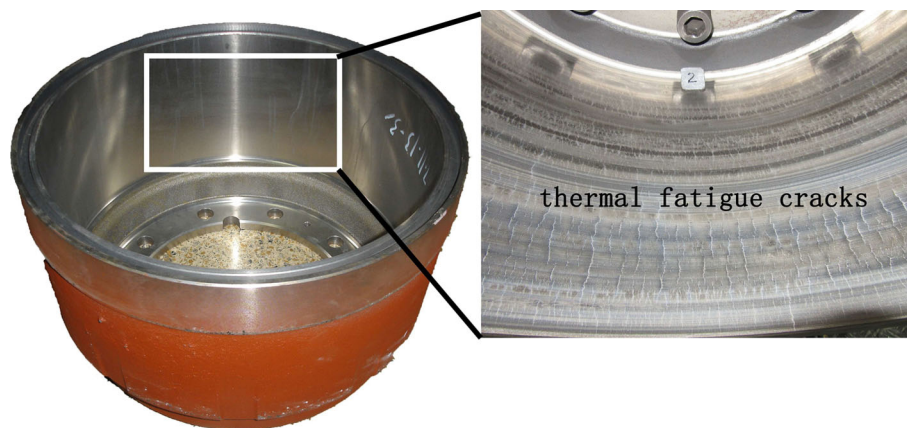

Fig. 1 Schematic diagram of thermal fatigue cracks on brake drum working surface
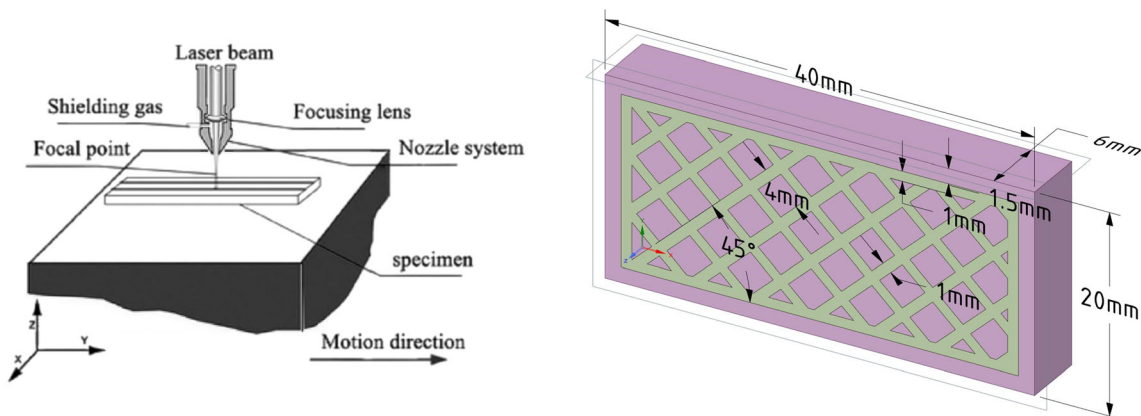

Fig. 2 Schematic of laser processing and double combination model

be able to hang the samples on the hanging plate of the thermal fatigue test machine. Subsequently, all samples were polished with sandpaper (from 80# to 1000#). The double combination model on the sample surface was treated by a pulsed laser. A Nd-YAG pulsed laser welding machine (emitting laser wavelength 1.06 m, maximum power 800 w) is used to fabricate the laser melting surface of double binding, with a neodymium-doped yttrium aluminum garnet crystal as the working material. The five laser parameters are as follows: current 137 (A), pulse width 6 (ms), frequency 4 (Hz), defocusing distance +6.5 (mm) and speed of the laser head 1.2 (mm/s).

The laser melting surface used in this paper is a double combination pattern, that is, the combination of one circle along the perimeter of the sample (called anti-crack ring) and a 45°angle mesh; the pattern and individual dimensions are shown in Fig. 2. The advantage of this pattern is that the anti-crack ring which is perpendicular to the growth direction of the thermal fatigue crack can impede the crack to the greatest extent, and the mesh model can limit the crack to a specific range and cut off its growth path (Ref 20).

2.3 Testing Method

The pearlite contents and spacing of different parts of brake drum were observed by optical microscopy (Zeiss, Axio Imager, A2m, Germany) and scanning electron microscopy (SEM) after being etched in a 4% nitric acid alcohol solution. The pearlite content was determined via automatic image analysis (Zeiss, AxioVision) and ISO standard (Ref 21). Samples with different interlamellar spacings were measured by the improved secant method (Ref 22). A number of straight lines are drawn on the photographs that need to be measured. The straight lines need to go through the whole picture, count the number of interlaminar points that intersect with each line, and measure the length of the line. The length of the non-pearlite part cannot be counted. The formula for measuring the average interlamellar spacing is

$$\overline{d_0} = \frac{4}{\Pi^2}\overline{L} \qquad \text{(Eq 1)}$$

$$\overline{L} = \frac{L}{n \times M} \qquad \text{(Eq 2)}$$

where L is the sum of all secant segments passing through the pearlite, n is the number of intersection points between all secants and interlamellar, M is the magnification factor of the microscope and $\overline{d_0}$ is the average interlamellar spacing.

Next, a Rigaku x-ray diffractometer was used to calibrate the phase composition of the untreated and the treated samples. In addition, Buehler automatic microhardness tester was used to measure the microhardness of the pearlite matrix of all samples; the hardness tester indenter is a quadrilateral conical diamond with a load of 0.2 kg and a holding time of 10 s. Each sample is measured five times, and the results were averaged over five microhardness values.

The thermal fatigue experiments in this paper were all carried out by a self-made thermal fatigue machine, as shown in Fig. 3. The furnace is made of 310s stainless steel. The thermal fatigue machine used a connecting rod and other devices to control the vertical movement of the pallet carrying the samples. All samples were suspended from the tray by a wire so that they are at the same height. The air temperature is controlled by a temperature controller, the temperature is measured by a k-thermocouple, and the heating and cooling time is controlled by an electromagnetic relay. The samples were circulated between 700°C and 25°C for heating and cooling of 180s and 5s, respectively. After stopping the experiment every 200 cycles, the samples were taken off one by one and soaked in a 3% hydrochloric acid solution. In this way, the oxide layer on the surface could be removed, and the samples could be observed more accurately and prepared for the wear experiments. The specimen was then immersed in an anhydrous ethanol solution, cleaned by ultrasound for 20 minutes and dried by a dryer or left to dry naturally, and finally the number and length of the thermal fatigue cracks were observed and recorded.

The wear testing is performed with a self-made linear reciprocating sliding friction and wear tester, as shown in Fig. 4. The counter section is made of steel 45# with a hardness of 50 HRC. The test conditions are: load 60N, rotation speed 700 RPM and wear time 60 h. After every 200 thermal fatigue tests, wear tests were carried out on all samples to determine the weight loss of the samples. The weight loss of the worn samples was determined by weighing the samples before and
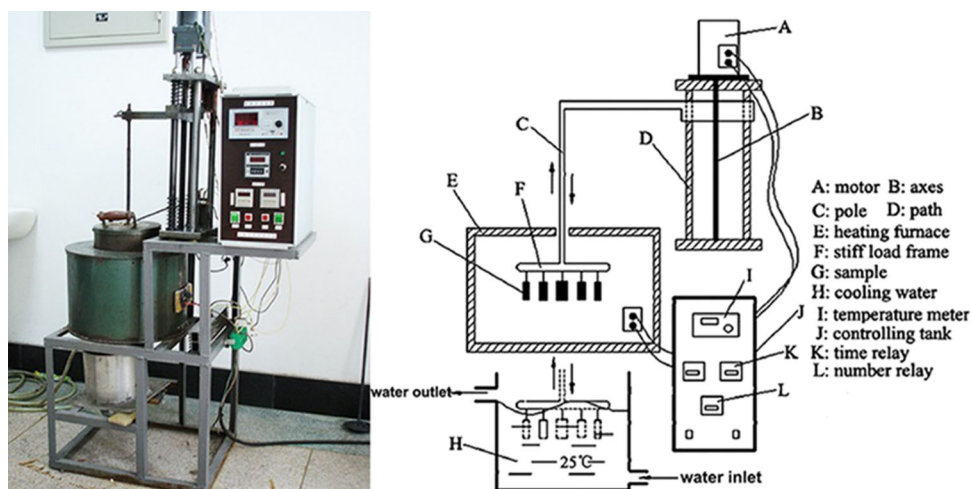

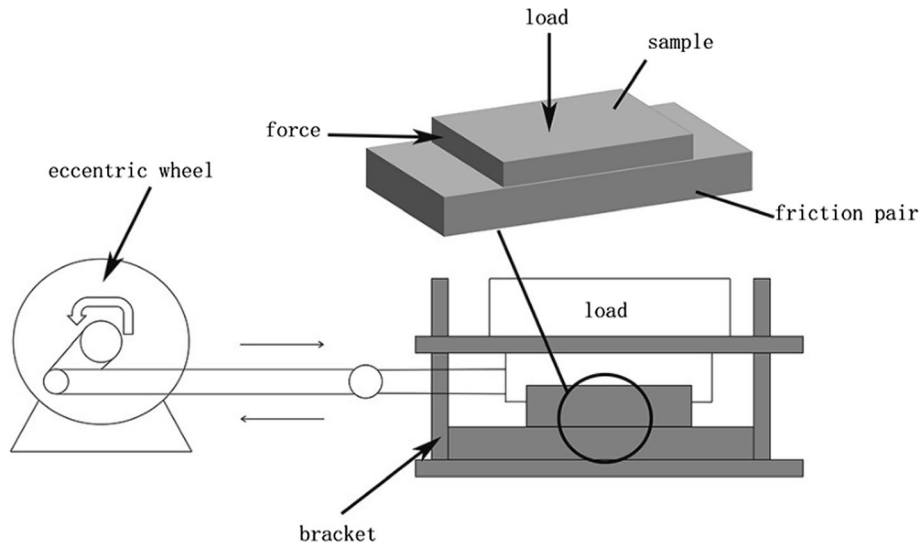**Fig. 3** Sketch of the thermal fatigue testing machine

A: motor B: axes
C: pole   D: path
E: heating furnace
F: stiff load frame
G: sample
H: cooling water
I: temperature meter
J: controlling tank
K: time relay
L: number relay

Fig. 4 Self-made linear reciprocating sliding friction and wear tester
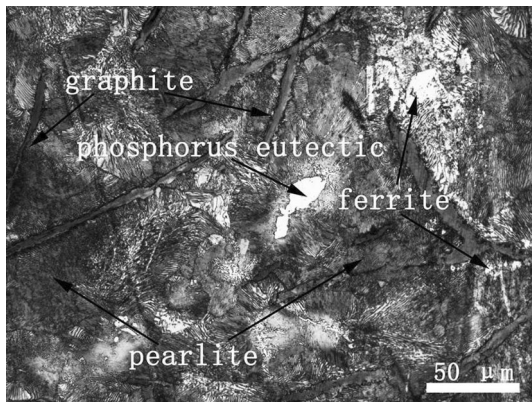

Fig. 5 The metallographic picture of gray cast iron

after the wear test with an electronic balance with an accuracy of 0.001g.

The finite element analysis software Ansys 2020 R2 was used to investigate the stress distribution on the surface of untreated and treated samples.

3. Results and Discussion

3.1 Pearlite

The metallographic picture of gray cast iron is shown in Fig. 5. After etching, the dark black part is pearlite, the shiny white part is ferrite, and erratic dendrite is phosphorus eutectic (Ref 23). The flake-shaped phase with irregular direction is graphite. According to the picture, it can be seen that the pearlites are layered like terraces (Ref 24).

The pearlite contents of the samples are listed in Table 1, and the metallographic pictures of each sample are shown in Fig. 6 and 7. As the automatic image analysis software is based on the quantitative analysis of the extraction of different microstructures presented in different grayscales after corrosion, it is not possible to identify pearlite with large interlamellar spacing, as it appears white in the microscope after

etching. The pearlite contents in different regions of the brake drum are different because the thickness of the casting wall is closely related to the cooling rate during the casting process (Ref 25). The brake drum flange is the thickest at the bottom, and the wall becomes gradually thinner toward the top. When the wall thickness decreases and the cooling rate increases, the graphite becomes finer, pearlite fraction increases, and the strength and hardness increase. On the contrary, if the wall thickness is thick and the cooling rate is slow, the graphite becomes coarse and ferrite content increases, and the strength and hardness decrease.

Figure 7 shows an optical microscopy image with a 1000 times magnification. Due to the extremely small pearlite interlamellar spacing between S3 and S4 samples in Fig. 7, the optical microscope cannot meet the observation requirements, so the samples of S3 and S4 were additionally measured by scanning electron microscopy (SEM), as shown in Fig. 8. Through measurement, the average pearlite interlamellar spacing of the following four ranges was obtained as follows: 860nm, 720nm, 188nm and 152nm.

The interlamellar spacing of pearlite is determined by temperature (Ref 26). Pearlite formation occurs within a temperature range. Due to the high formation temperature of the first cooled pearlite, the C atom has a fast diffusion rate, a long diffusion distance and a large pearlite interlamellar spacing. As the temperature decreases, the pearlite obtained after cooling increases due to the rise of condensate depression degree, the nucleation rate increases, and the diffusion velocity and distance of C atoms decrease, resulting in the reduction in interlamellar spacing.

3.2 Unit

A single point fabricated with appropriate laser parameters is called a unit. Figure 9(a) shows a picture of a cross section of the unit, and Fig. 9(b) shows the junction of the base and the unit. It can be seen from the figure that the treated sample is divided into three parts. The morphologies of the unit can be clearly distinguished by optical microscope, while the transformed zone at the junction of the unit and the base needs to be observed by scanning electron microscope. The boundary

Table 1 Pearlite contents, interlamellar spacing and microhardness of all samples

Sample	Pearlite contents (Pearlite+Ferrite=100%)	Pearlite interlamellar spacings	Microhardness(HV)
A	≤ 45%	865nm	292
B	45~55%	792nm	299
C	55~65%	813nm	302
D	65~75%	832nm	308
E	75~85%	736nm	316
F	≥ 85%	745nm	323
S1	65~75%	860nm	307
S2	75~85%	720nm	316
S3	65~75%	188nm	343
S4	75~85%	152nm	352
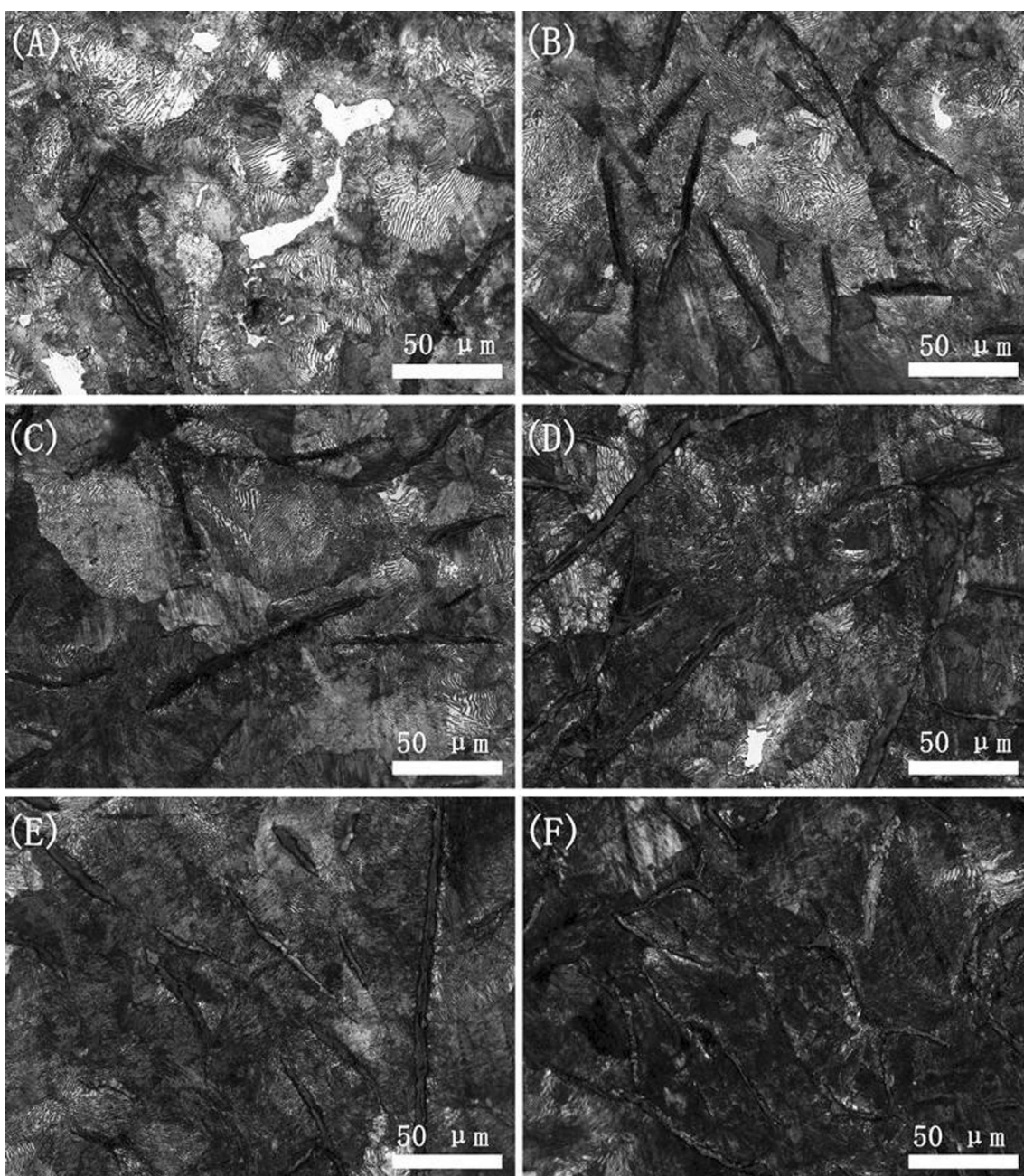
Fig. 6 Metallographic pictures of different pearlite contents. (a) Pearlite contents ≤ 45%; (b) pearlite contents 45%~55%; (c) pearlite contents 55%~65%; (d) pearlite contents 65%~75%; (e) pearlite contents 75%~85%; (f) pearlite contents ≥ 85%
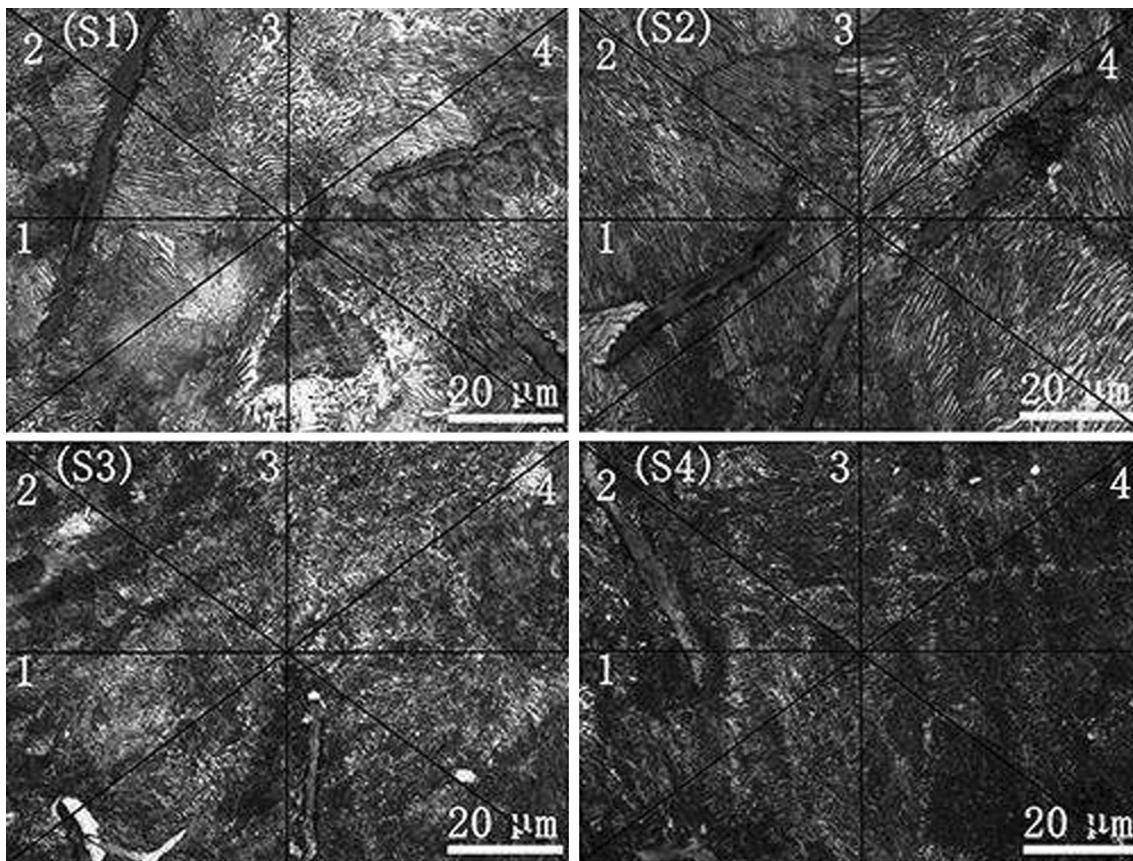
Fig. 7 Metallographic pictures of different pearlite interlamellar spacings. (S1) 860nm; (S2) 720nm; (S3) 188nm; (S4) 152nm
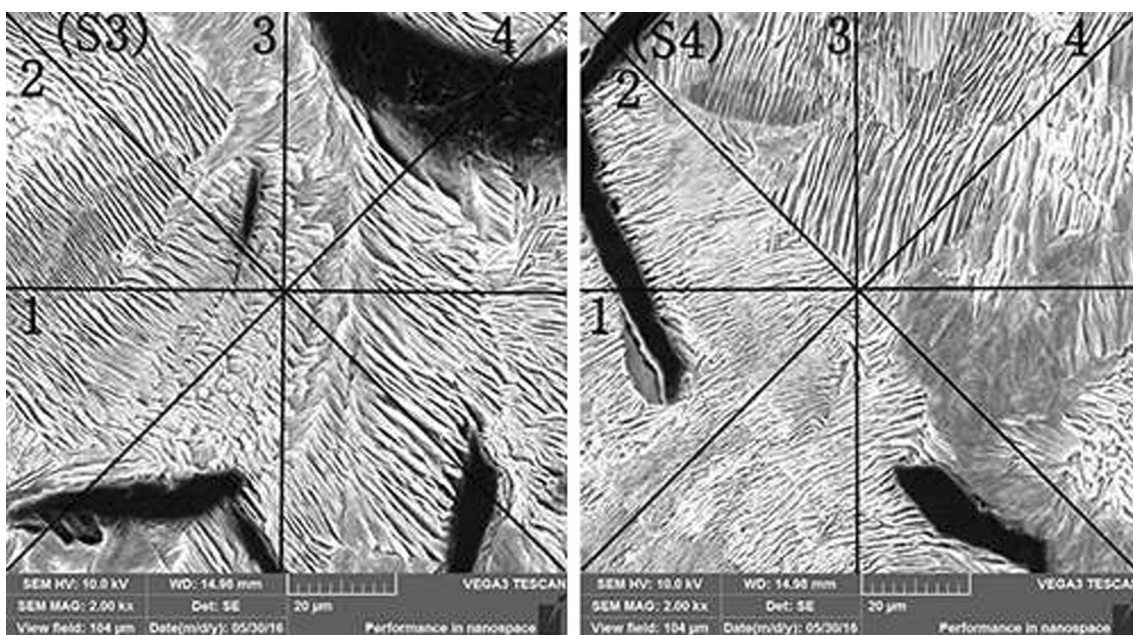

Fig. 8 Metallographic pictures of different pearlite interlamellar spacings obtained by SEM. (S3) 188nm; (S4) 152nm

between each zone is obvious, no graphite is present in the melted zone, and the grain size is significantly refined. The transformed zone retains less graphite than the base zone.

The phase analysis of the unit and matrix was performed by x-ray diffraction. The result is shown in Fig. 10. According to the diffraction peak calibration result, the gray cast iron base contains graphite and ferrite. After laser treatment, the corresponding peak of the ferrite became broader, and the martensite, cementite and residual austenite were identified by calibration. It confirms that the fine microstructure is a mixture
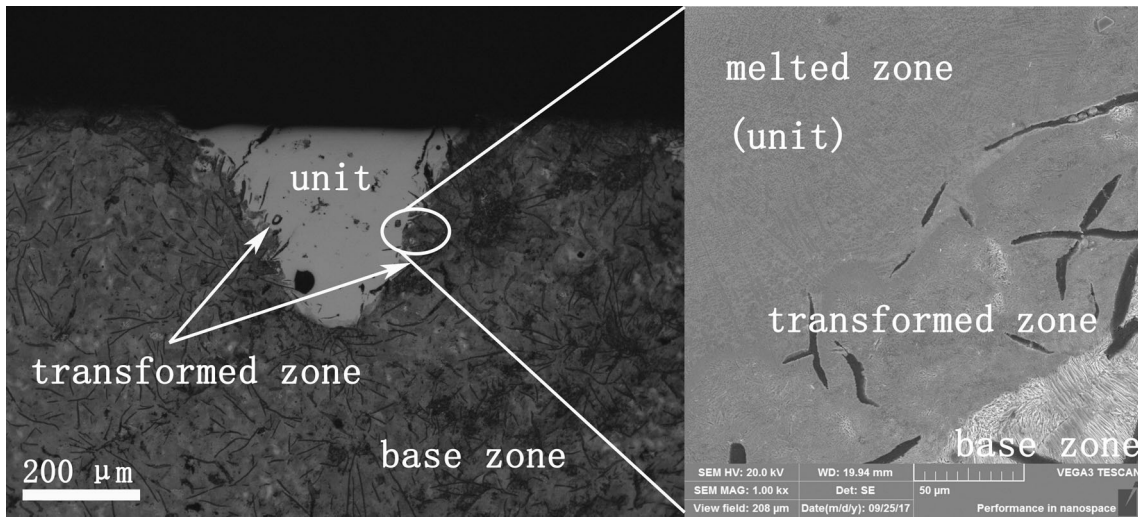
Fig. 9 The microstructure of unit and base. (a) Cross-section of unit and base; (b) junction of the base and unit
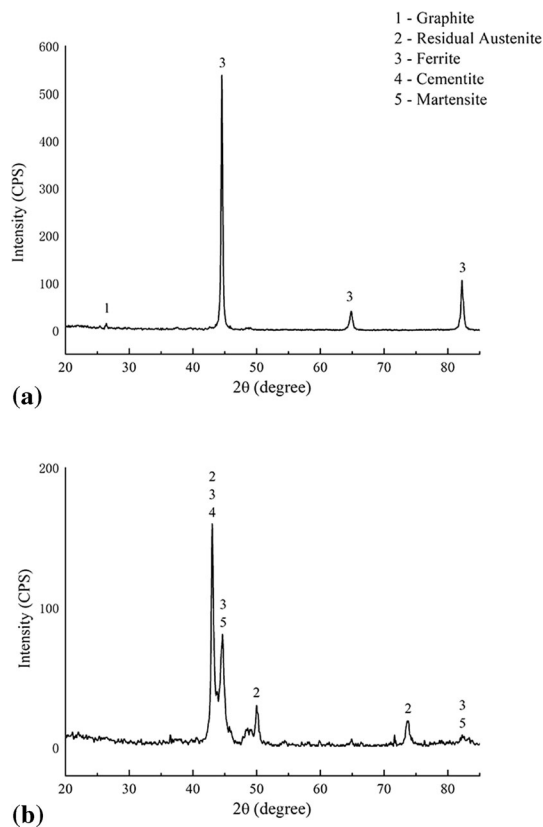

(a)

(b)

Fig. 10 X-ray diffraction: (a) the untreated sample; (b) the treated sample

of martensite, residual austenite and ledeburite, which is also a mixture of cementite, martensite and residual austenite. The microstructure of ledeburite in the laser-melted zone is shown in Fig. 11. After the partial melting of the matrix gray cast iron irradiated by laser, the graphite was completely dissolved. Because of the fast cooling rate and the large degree of supercooling, the nucleation rate was much higher than the growth rate of the crystal nucleus, and the fine microstructure was obtained. The temperature during laser processing is close
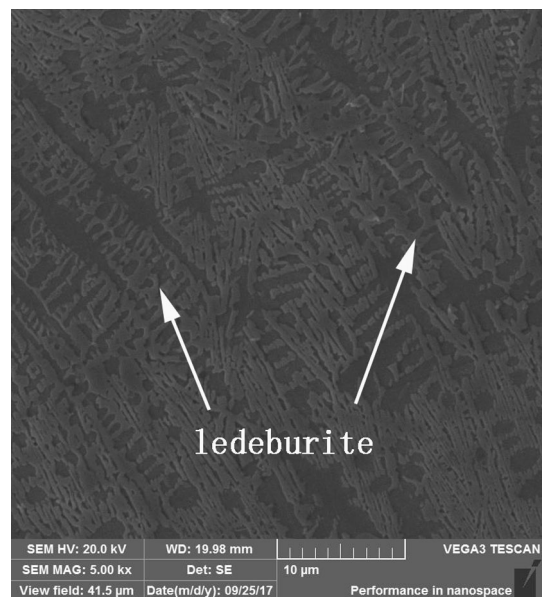

Fig. 11 Microstructure of ledeburite in the laser-melted zone

to the melting point of gray cast iron, which corresponds to a solid-state phase change around the melt solidification zone, hence the name transformed zone, where the austenitizing process is very rapid and some of the graphite dissolves.

3.3 The Microhardness of Base and the Unit

Microhardness measurements were taken after the laser treatment because the laser treatment changes the microstructure.

The base and unit hardness of the samples with different pearlite contents are shown in Fig. 12. Two different patterns are used to represent the base and unit, respectively. The vertical ladder is used to show the difference in hardness between the samples more clearly. Basically, the hardness of the unit of all samples is much higher than that of the base, and the hardness of the unit of each sample does not differ much. The
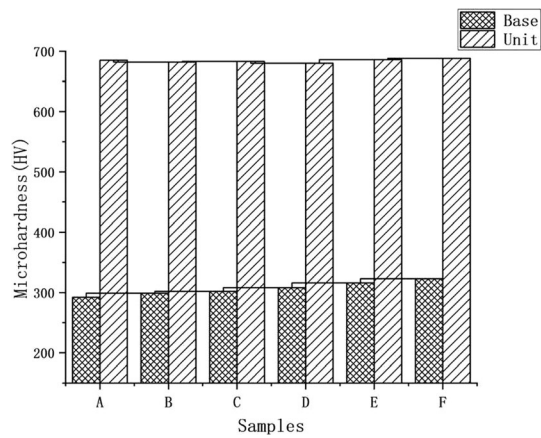
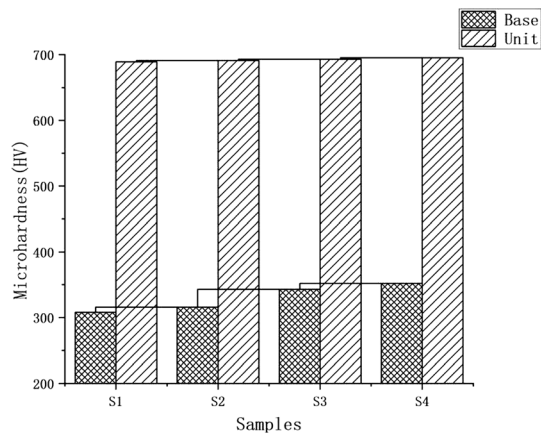**Fig. 12** Microhardness of different pearlite contents

Fig. 13 Microhardness of different pearlite interlamellar spacings

hardness of the base of each sample shows an increasing trend from A to F.

The reason why the base hardness is different is that the pearlite contents are different. Because pearlite is a mechanical mixture of ferrite and cementite (Ref 27), it has higher strength and hardness, so the samples with more pearlite have higher hardness. There is no significant difference in the hardness of the unit when comparing all the samples, because the base area treated by the laser melts, and the solid phase transition occurs in a small surrounding area, all of the graphite dissolves, and then the melting area cools rapidly to obtain the finer structures such as martensite and ledeburite.

Figure 13 shows the microhardness results of samples with different pearlite interlamellar spacings. The hardness of the unit in Fig. 13 is all much higher than that of the base, and the hardness of the unit of each sample is very similar. The hardness of the base S1 and S2 is close to each other, the hardness of S3 and S4 is close to each other, and the hardness of S3 and S4 is greater than that of S1 and S2. Sample S4 with the smallest spacing has the highest hardness. The reason for this result is that the mechanical properties of the pearlite depend on the pearlite spacing. The smaller the pearlite spacing, the higher the strength and hardness. However, it can be seen that the hardness after laser treatment is related to the unit itself; it does not depend on the interlamellar spacing before the laser treatment.

3.4 Thermal Fatigue Test

In this paper, thermal fatigue tests were conducted to observe and count the quantity of cracks and the main crack length of samples every 200 cycles. Since the thermal fatigue crack of the brake drum is macroscopically visible, the crack must be greater than or equal to 1 mm.

3.4.1 Thermal Fatigue Test Results of Different Pearlite Contents. The thermal fatigue tests were first conducted on samples with different pearlite contents. According to the results shown in Fig. 14(a), the quantity of cracks increases with the increase in thermal fatigue cycles, but the growth rate is not the same. It can be concluded from the figure that when the thermal fatigue cracking is observed for 200 cycles at the first time, the quantity of cracks in sample A with the lowest pearlite quantity is the largest, while in sample F with the highest pearlite content it is the smallest. The quantity of thermal fatigue cracks began to converge when the test was conducted for 600 cycles, and the growth rate of the number of cracks in all samples between 600 and 800 cycles was similar and tended to be flat. In Fig. 14(b), the quantity of cracks from samples A–F goes from more to less, and the quantity of cracks in all samples at each stage is less than that in Fig. 14(a).

The following results can be obtained by looking at the main crack length results in Fig.15(a). At the end of the experiment, the main crack length on the surface of all the samples was similar, and the stage of the fastest crack growth was 600 to 800 cycles. When the cycle was from 200 to 400, the difference in the length of the main crack between samples was the largest, with sample A having the longest main crack and sample F the shortest. For the treated samples shown in Fig. 15(b), the anti-crack ring played a great role in preventing crack growth due to the small number of thermal cycles at 200 cycles. Subsequently, although the crack continued to grow, the overall crack length was much shorter than that of untreated samples and approached the width (20 mm) of the test sample.

The generation of a thermal fatigue crack is due to the thermal stress generated by the change in temperature, which deforms the material and leads to the cracking or even destruction (Ref 28). For gray cast iron, stress concentration at the graphite tip is the leading crack initiation site. The crack starts from the graphite tip and grows by connection with other graphite tip cracks (Ref 29). Pearlite, because of its high hardness and high strength, can resist the initial small thermal stress. As can be seen from Fig. 16, the crack is generated at the graphite tip. Due to the pearlite, the crack growth is hindered, and the direction of the crack growth is affected by the direction of the lamellar pearlite, so that the crack has to bridge with another graphite flake for a longer distance. It is because of the role played by pearlite in the early stage of the thermal fatigue test, that is, sample F with 90% pearlite has the least quantity of cracks and the shortest main crack. Also, at the later stage of the experiment, the crack continued to expand, pearlite was decomposed, and hardness was reduced (Ref 30), and many small crack bridges joined to form the main crack. The microstructure under different thermal cycles is shown in Fig. 17, the content becomes less and less, and the ferrite increases as the thermal cycle increases. Finally, at the end of the test, the main crack of all samples grew to the limit value.

Since the crack mainly originates at the graphite tip, after laser treatment, the microstructure of the fused area is all dissolved (Ref 31), so the unit itself limits crack initiation. The thermal fatigue test results of the treated samples were much
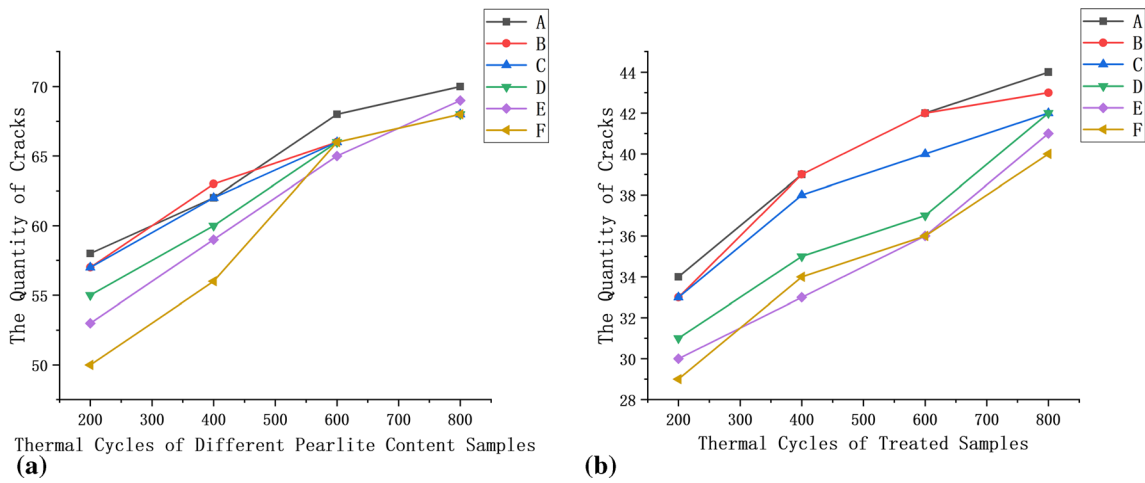
Fig. 14 The quantity of thermal fatigue cracks of different pearlite contents. (a) Untreated samples; (b) treated samples
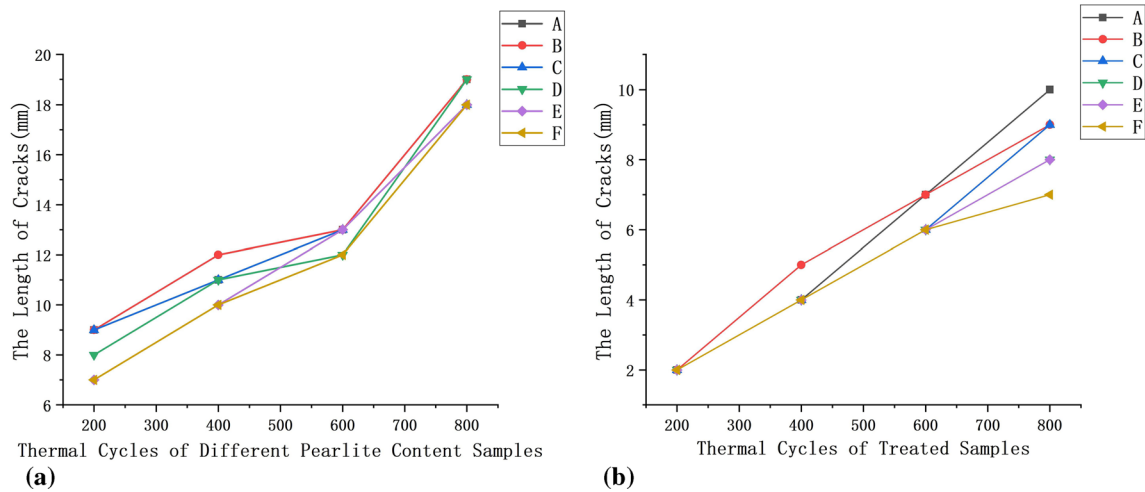

Fig. 15 The main crack length of different pearlite contents. (a) Untreated samples; (b): treated samples
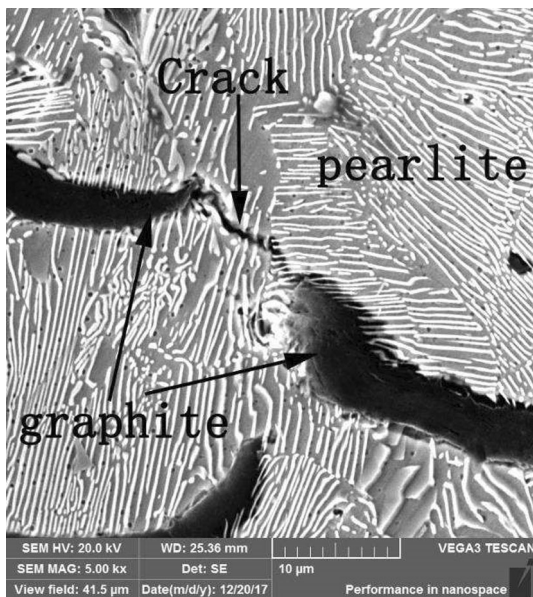

Fig. 16 The propagation of thermal fatigue crack

better than those of the raw samples. In the early stage of the experiment, the thermal fatigue cracks were all generated at the sample boundary, and the model with an angle of 0°parallel to the sample boundary hindered the crack propagation. With the progress of the experiment, the mesh model not only delays the initiation of cracks but also restricts the growth of cracks in the mesh.

3.4.2 Thermal Fatigue Test Results of Interlamellar Spacing of Pearlite. Four samples with the different interlamellar spacing of pearlite were subjected to thermal fatigue testing, and the quantity of cracks and the length of main cracks were observed every 200 cycles. As can be seen from the results shown in Fig. 18(a), the quantity of cracks in the four samples was from maximum to minimum S1 > S2 > S3 > S4 at 200 cycles. As the experiment continued, the quantity of cracks in S1 and S2 was the same, and the number of cracks in S3 and S4 was the same. In Fig. 18(b), the quantity of cracks in the four samples in each cycle is smaller than that in Fig. 16(a) and the quantity of cracks in S3 and S4 is slightly smaller than that in S1 and S2 at the end of the experiment.

As for the main crack length in Fig. 19(a), it can be seen that S1 has the most extended crack at 200 cycles, S2 has the second longest, and S3 is the same as S4 with the shortest main
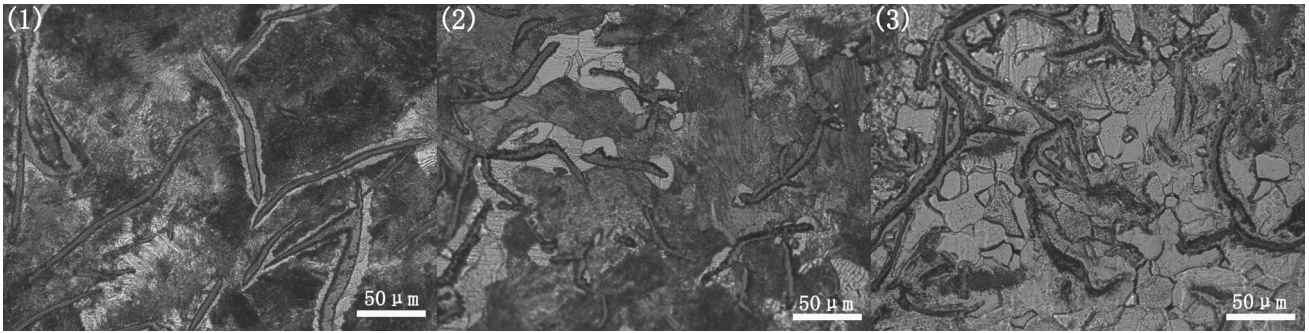
Fig. 17 Microstructure of gray cast iron under different thermal fatigue cycles: (1) 200 cycles; (2) 400 cycles; (3) 600 cycles
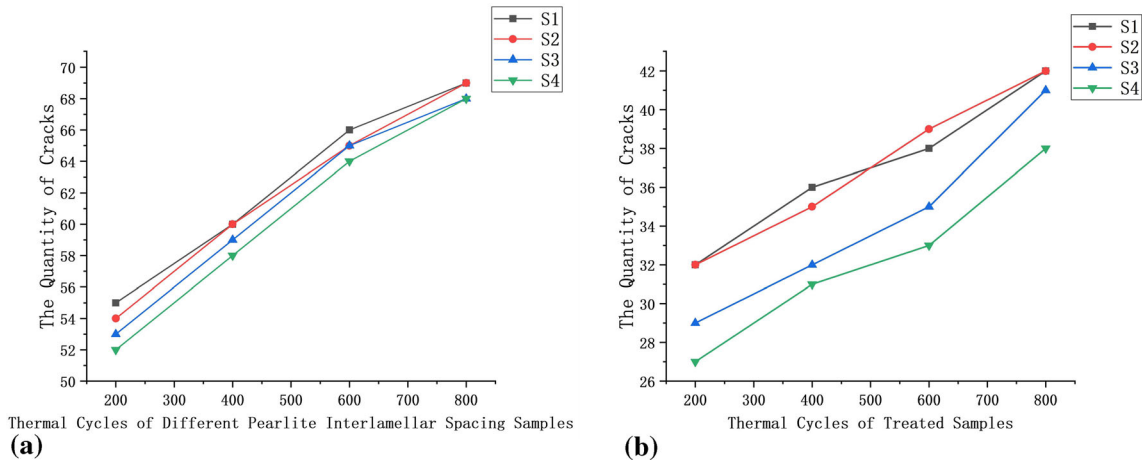

Fig. 18 The quantity of thermal fatigue cracks of different pearlite interlamellar spacings. (a) Untreated samples; (b) treated samples
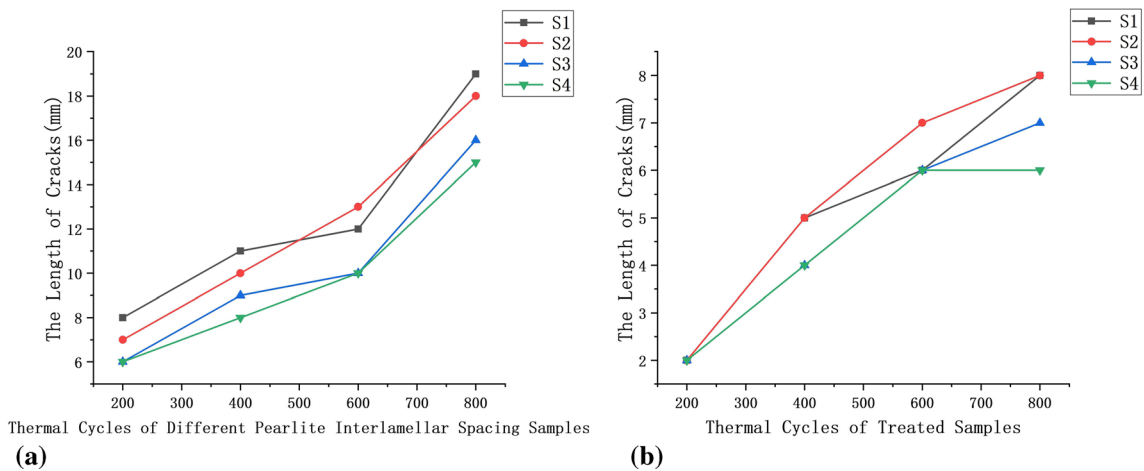

Fig. 19 The main crack length of different pearlite interlamellar spacings. (a) Untreated samples; (b) treated samples

crack. The growth rate of the main crack was the fastest during cycling from 600 to 800, and the final length of the main crack was S1 > S2 > S3 > S4 from long to short. The results of the treated samples are shown in Fig. 19(b). The main crack length of all samples was limited to 2mm after 200 cycles. The main crack length of S3 and S4 at 800 cycles was smaller than S1 and S2, and the main crack length of all samples was much smaller than that of the samples in Fig. 19(a).

Since the mechanical properties of pearlite depend on the interlamellar spacing (Ref 32), more thermal stress is needed for crack growth to break through the pearlite with smaller interlamellar spacing. Therefore, considering both the quantity of cracks and the length of cracks, S3 and S4 with shorter spacing had fewer and shorter cracks than S1 and S2. Compared with the results of samples with different pearlite quantities, different interlamellar spacings can better reflect the

performance of pearlite. Before 600 cycles, the growth rate of the main crack was slow, which was attributed to the excellent performance of the pearlite. However, during cycling between 600 and 800 cycles, with the decrease in pearlite and the increase in ferrite, the crack growth rate became faster. Figure 20 shows how the mesh hinders the thermal fatigue crack. When touching the mesh, the crack was first passivated (Ref 33), and with the increase in thermal fatigue cycling, the crack bifurcated and deflected along the boundary of the mesh in two opposite directions, the crack expansion path is extended, and the thermal fatigue resistance of the sample is also increased, while more energy needs to be accumulated in the original direction of crack growth to break through the mesh pattern, and grow in the original direction of crack accumulation energy.

3.5 Wear Test

The main failure form of the brake drum of gray iron is thermal fatigue cracking, and the heat comes from the friction between the brake drum and the brake shoes, so the wear performance of the samples must be tested. In this paper, the wear loss weight of the sample is used to judge the wear performance, and the wear mechanism of the treated samples is discussed by using finite element software to analyze the stress distribution of the surface.

Figure 21 shows the equivalent stress distribution of untreated and treated samples. In the figure, the closer to red, the higher the stress value; the closer to blue, the lower the stress value. For the untreated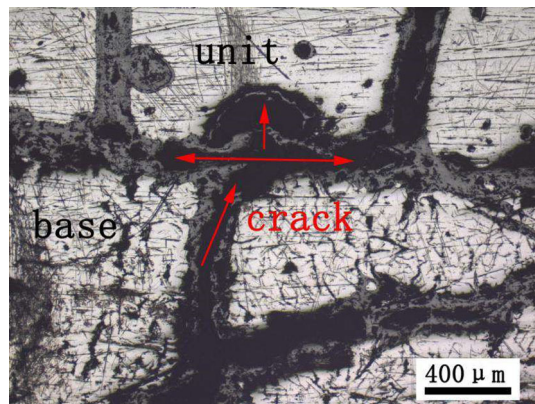 sample, the stress at edges is relatively concentrated, maximum stress up to 0.21792Mpa, while the stress at the rest of the surface is small and average. As for Fig. 21(b), the stress is concentrated on the laser melting pattern; the maximum stress is only 0.073701Mpa. According to the wear results, the wear weight loss trend of the samples with different pearlite contents is roughly the same in Fig. 22(a). The weight loss at 200 cycles is inversely proportional to the pearlite content, which is because the microhardness of the samples with a large quantity of pearlite is relatively large, and the pearlite can exert specific wear resistance. With the development of the thermal fatigue experiment, the pearlite content decreased and gradually decomposed into ferrite, the hardness declined, the wear resistance also decreased, and the wear amount increased significantly. By observing the results of the treated sample in Fig. 22(b), the following conclusions can be drawn: The treated sample is not only effective against thermal fatigue cracking but also can increase the wear resistance of the sample, and the weight loss of the treated sample is far lower than other samples. This is because the stress is mainly distributed on the treated model with higher hardness, which acts as a support and protection for the rest of the surface.

According to Fig. 23a, S3 and S4 with smaller interlamellar spacing have less weight loss than S1 and S2, indicating that the sample with smaller spacing has better wear resistance. In Fig. 23b, the treated samples' results follow the same rule, where weight loss in every stage of every sample was less than for untreated samples. In addition, it can be seen that samples D and E behave very similarly to S1 and S2, and likewise S3 and S4 behave very similarly except that the interlamellar spacings are smaller for the S3 and S4 samples.

For the treated samples, the samples with a finer pearlite interlamellar spacing also act in a supporting role in the early stage of the experiment. Generally, the wear resistance of treated samples is much better than that of untreated samples. It can be seen from the results at the end of the experiment that the treated surface could still improve the wear resistance when the pearlite effect almost disappears.

At present, there is no research on the effect of pearlite quantity and interlamellar spacing on the thermal fatigue and wear resistance of laser-treated gray cast iron, so this paper has a certain research significance and reference value for industrial applications.
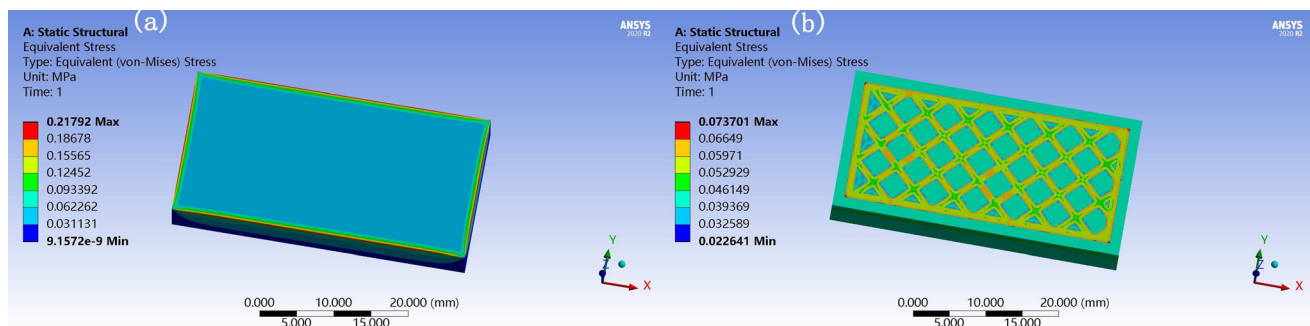

Fig. 20 The mesh hinders the growth of thermal fatigue crack

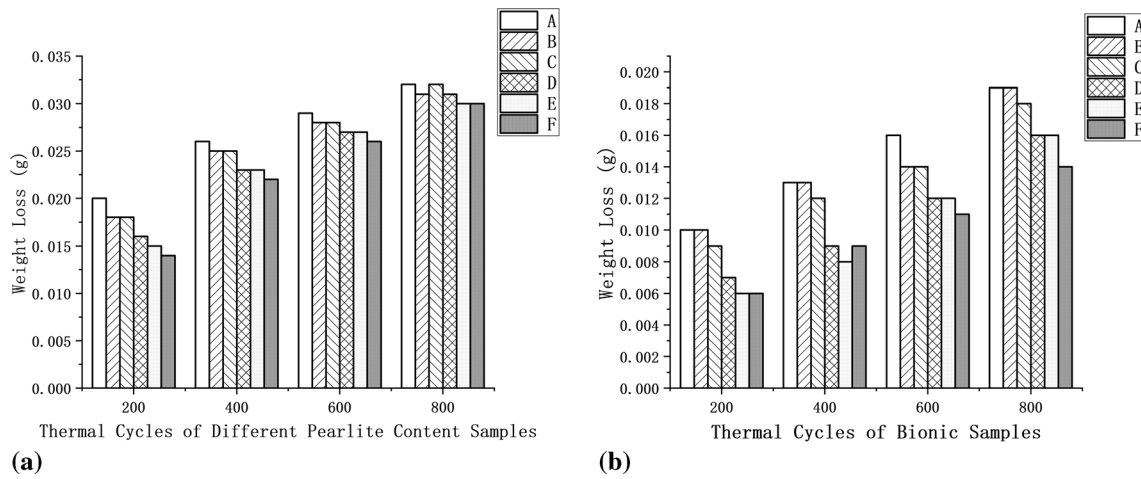**Fig. 21** The equivalent stress distribution. (a) Untreated sample; (b) treated sample.

Fig. 22 Weight loss of different pearlite contents. (a) Untreated samples; (b) treated samples
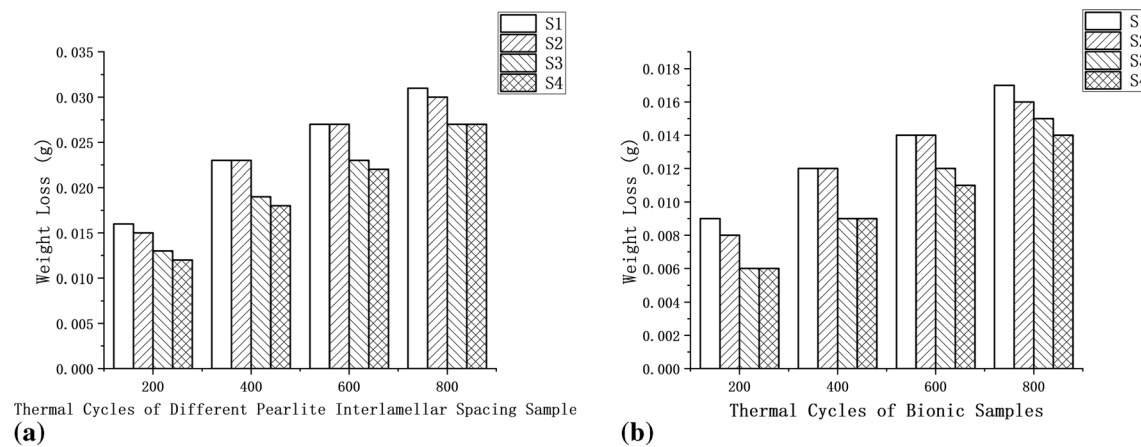

Fig. 23 Weight loss of different pearlite interlamellar spacings. (a) Untreated samples; (b) treated samples

4. Conclusions

In the present study, to increase the service life of gray cast iron brake drums and reduce the production cost, the effect of laser treatment on thermal fatigue and wear resistance of gray cast iron with different pearlite contents and different interlamellar spacings was explored. The improvement in thermal fatigue and wear resistance of pearlitic gray cast iron has been achieved with a 45°mesh double combination model, and the following conclusions are summarized.

The thermal fatigue and wear resistance of pearlitic gray cast iron samples with varying pearlite contents are different; the more the pearlite, the better the thermal fatigue and wear resistance. The pearlitic gray cast iron samples with different interlamellar spacings had different thermal fatigue and wear resistance values; the smaller the interlamellar spacing, the better the thermal fatigue and wear resistance. However, with the thermal fatigue experiment, the pearlite will gradually decompose, and the pearlite's function will gradually disappear in the later stage of the experiment.

Due to the existence of ledeburite, martensite and residual austenite in the laser melting zone, it had a significantly higher hardness. Meanwhile, in the wear test, finite element analysis of the samples' surface revealed that the stresses were mainly distributed on the laser melting model. The thermal fatigue and wear resistance of the treated samples are better than those of the untreated samples. This research suggests that the 45° mesh double combination model can double the service life of a cast iron truck brake drum.

For untreated and treated samples, with pearlite contents greater than or equal to 85%, and with pearlite interlamellar spacing of 152nm, the best thermal fatigue and wear resistance were obtained. After laser processing, the influence of pearlite fraction was reduced, and the difference between the experimental results of each sample was reduced, which is better than that of the untreated samples.

Conflict of interest

The authors declared that there is no conflict of interest.

References

1. Y. Sato, Y. Yuasa, Y. Akagawa, et al. An Investigation of Preferable Taper and Thickness Ratios for Cast Circumferential Clasp Arms using Finite Element Analysis. *Int. J. Prosthodont.* 1995; 8: 392-397. 1995/07/01

2. S. Pan, F. Zeng, N. Su et al., The Effect of Niobium Addition on the Microstructure and Properties of Cast Iron Used in Cylinder Head, *J. Mater. Res. Technol. Jmr&T*, 2020, **9**, p 1509–1518. https://doi.org/10.1016/j.jmrt.2019.11.076

3. M. Lou and A.T. Alpas, Characterization of Lubricated Friction Behavior of Thermal Spray Steel Coatings in Comparison with Grey Cast Iron, *Lubricants*, 2020 https://doi.org/10.3390/lubricants8010009

4. O.P. Singh, S. Mohan, K.V. Mangaraju et al., Thermal Seizures in Automotive Brake Drums, *Eng. Fail. Anal.*, 2010, **17**, p 1155–1172. https://doi.org/10.1016/j.engfailanal.2010.02.001

5. M. Yan and J. Xu, Prediction Model for Brake-Drum Temperature of Large Trucks on Consecutive Mountain Downgrade Routes Based on Energy Conservation Law, *Math. Prob. Eng.*, 2018 https://doi.org/10.1155/2018/4587673

6. Y.-S. Feng, Z.-S. Ji, H.-S. Wu et al., Effects of Cooling Rate on Vermicular Graphite Percentage in a Brake Drum Produced By One-Step Cored Wire Injection, *China Foundry*, 2015, **12**, p 349–353

7. A. Josan, C. P.Bretotean, S. Ratiu S. Researches and Studies Regarding the Casting of Brake Drums From Cast Iron. In: Lemle LD (ed) *International Conference on Applied Sciences*. 2019

8. P. H. Tjahjanti, W. H. Nugroho, H. C. Wahyuni, Physics and Chemistry Test on Aluminum-Based Composite Materialsas an Alternative Material for The Manufacture of Brake Drum. In: Yuwono AH (ed) *Advances in Materials, Processing and Manufacturing*. 2013, pp.449-+

9. P. Yi, Y. Liu, C. Fan et al., Impact Analysis of the Thermal Mechanical Coupling Characteristics of Graphite Morphologies During Laser Cladding of Gray Cast Iron, *Opt. Laser Technol.*, 2017, **90**, p 52–64. https://doi.org/10.1016/j.optlastec.2016.11.011

10. G. B-c and C.-h Lim, Thermal Fatigue of Cast Iron Brake Disk Materials, *J. Mech. Sci. Technol.*, 2012, **26**, p 1719–1724. https://doi.org/10.1007/s12206-012-0435-2

11. H.Y. Wang, Z.D. Zhang and L.M. Liu, The Effect of Galvanized Iron Interlayer on the Intermetallics in the Laser Weld Bonding of Mg to Al Fusion Zone, *J. Mater. Eng. Perform.*, 2013, **22**, p 351–357. https://doi.org/10.1007/s11665-012-0260-x

12. P. Yi, P. Xu, C. Fan et al., Microstructure Formation and Fracturing Characteristics of Grey Cast Iron Repaired Using Laser, *Sci. World J.*, 2014 https://doi.org/10.1155/2014/541569

13. H. Zhou, X. Tong, Z. Zhang et al., The Thermal Fatigue Resistance of Cast Iron with Biomimetic Non-Smooth Surface Processed by Laser with Different Parameters, *Mater. Sci. Eng. a-Struct. Mater. Prop. Microstruct. Proc.*, 2006, **428**, p 141–147. https://doi.org/10.1016/j.msea.2006.04.101

14. X. Tong, H. Zhou, W. Zhang et al., Thermal Fatigue Behavior of Gray Cast Iron with Striated Biomimetic Non-Smooth Surface, *J. Mater. Process. Technol.*, 2008, **206**, p 473–480. https://doi.org/10.1016/j.jmatprotec.2007.12.043

15. H. Lu, M. Liu, D. Yu et al., Effects of Different Graphite Types on the Thermal Fatigue Behavior of Bionic Laser-Processed Gray Cast Iron, *Metallurg. Mater. Trans. a-Phys. Metallurg. Mater. Sci.*, 2018, **49A**, p 5848–5857. https://doi.org/10.1007/s11661-018-4885-8

16. D. Yu, T. Zhou, H. Zhou et al., Non-Single Bionic Coupling Model for Thermal Fatigue And Wear Resistance Of Gray Cast Iron Brake Drum, *Opt. Laser Technol.*, 2019, **111**, p 781–788. https://doi.org/10.1016/j.optlastec.2018.09.016

17. Y. Li, Y. He, J. Liu et al., Phase Transformation and Microstructure Evolution of Pearlite Heat-Resistant Steel During Heating, *Mater. Sci. Technol.*, 2020, **36**, p 771–782. https://doi.org/10.1080/02670836.2020.1738071

18. B. Hu, X. Tu, H. Luo et al., Effect of Warm Rolling Process on Microstructures and Tensile Properties of 10 Mn Steel, *J. Mater. Sci. Technol.*, 2020, **47**, p 131–141. https://doi.org/10.1016/j.jmst.2019.12.026

19. W. Huang, C.-S. Wang, Y.-F. Chang et al., A Digital Evaluation Approach for Nodule Size Analysis of Pearlite Mixture Phase Structure in Steel, *Metallog. Microstruct. Anal.*, 2020 https://doi.org/10.1007/s13632-020-00650-5

20. Z. Chen, T. Zhou, R. Zhao et al., Influence of Carbon Pre-Coating Prior to Laser Deposition on Rolling Contact Fatigue of Gray Cast Iron, *J. Mater. Res.*, 2015, **30**, p 3104–3115. https://doi.org/10.1557/jmr.2015.288

21. ISO 945-1: Microstructure of cast irons—part 1: graphite classification by visual analysis, MOD. *International Standards Organization* (2008)

22. A. Kazakov, D. Kiselev, E. Kazakova et al., Quantitative Description of Microstructural Banding in Steels, *Mater.Perf. Charact.*, 2017, **6**, p 224–236. https://doi.org/10.1520/mpc20160009

23. T.A. Kop, J. Sietsma and S. Van der Zwaag, Dilatometric Analysis of Phase Transformations in Hypo-Eutectoid Steels, *J. Mater. Sci.*, 2001, **36**, p 519–526. https://doi.org/10.1023/a:1004805402404

24. Y.T. Zhou, S.J. Zheng, Y.X. Jiang et al., Atomic Structure of the Fe/Fe3C Interface with the Isaichev Orientation in Pearlite, *Phil. Mag.*, 2017, **97**, p 2375–2386. https://doi.org/10.1080/14786435.2017.1332434

25. M. Riebisch, C. Seiler, B. Pustal et al., Microstructure of As-Cast High-Silicon Ductile Iron Produced Via Permanent Mold Casting, *Int. J. Metalcast.*, 2019, **13**, p 112–120. https://doi.org/10.1007/s40962-018-0232-5

26. W. Hui, Y. Zhang, C. Shao et al., Effect of Cooling Rate and Vanadium Content on the Microstructure and Hardness of Medium Carbon Forging Steel, *J. Mater. Sci. Technol.*, 2016, **32**, p 545–551. https://doi.org/10.1016/j.jmst.2016.01.006

27. E.P. Vuorinen, A.G. Ozugurler, J.C. Ion et al., Hot Forming of Ultra-Fine-Grained Multiphase Steel Products Using Press Hardening Combined with Quenching and Partitioning Process, *Metals*, 2019 https://doi.org/10.3390/met9030357

28. C. Meng, H. Zhou, Y. Zhou et al., Influence of Different Temperatures on the Thermal Fatigue Behavior and Thermal Stability of Hot-Work Tool Steel Processed by a Biomimetic Couple Laser Technique, *Opt. Laser Technol.*, 2014, **57**, p 57–65. https://doi.org/10.1016/j.optlastec.2013.09.038

29. S. Ghodrat, A. Kalra, L.A.I. Kestens et al., Thermo-Mechanical Fatigue Lifetime Assessment of Spheroidal Cast Iron at Different Thermal Constraint Levels, *Metals*, 2019 https://doi.org/10.3390/met9101068

30. H. Zhou, P. Zhang, Z. Zhang et al., Thermal Cycling Effect on the Wear Resistance of Bionic Laser Processed Gray Iron, *J. Bionic Eng.*, 2014, **11**, p 288–295. https://doi.org/10.1016/s1672-6529(14)60031-7

31. T. Andriollo, Y. Zhang, S. Faester et al., Analysis of the Correlation Between Micro-Mechanical Fields and Fatigue Crack Propagation Path in Nodular Cast Iron, *Acta Mater.*, 2020, **188**, p 302–314. https://doi.org/10.1016/j.actamat.2020.02.026

32. S.-t Zhou, Z.-d Li, C.-f Yang et al., Cleavage Fracture and Microstructural Effects on the Toughness of a Medium Carbon Pearlitic Steel For High-Speed Railway Wheel, *Mater. Sci. Eng. a-Struct. Mater. Prop. Microstruct. Proc.*, 2019 https://doi.org/10.1016/j.msea.2019.138036

33. I.M. Dmytrakh, R.L. Leshchak and A.M. Syrotyuk, Influence of Sodium Nitrite Concentration in Aqueous Corrosion Solution on Fatigue Crack Growth in Carbon Pipeline Steel, *Int. J. Fatigue*, 2019 https://doi.org/10.1016/j.ijfatigue.2019.105192